PAPER

Check for updates

Role of the diffusion boundary layer in the molecular imprinting of PFAS in poly(*ortho*-phenylenediamine) toward improving MIP-based sensors

Cameron S. Malloy, Matthew J. Danley, Daniel A. Bellido-Aguilar,
Logan E. Chung and Suchol Savagatrup [iD] *

Molecularly imprinted polymers (MIPs) and electrochemical sensors offer a promising route for rapid and onsite detection of per- and polyfluoroalkyl substances (PFAS). The quantity and quality of the imprinted cavities in MIPs underpin the selective recognition and sensing performance of MIP-based sensors. Thus, understanding the role of various synthesis parameters during the electropolymerization of MIPs is crucial to control the imprinting process for various PFAS templates. Herein, we demonstrate that the synthesis scan rate used during electrosynthesis of MIPs can be leveraged to modulate the imprinting efficiency of PFAS with different tail lengths within a poly(*ortho*-phenylenediamine) (PoPD) film. Specifically, we test the hypothesis that increasing the scan rate, which reduces the thickness of the diffusion boundary layer during electropolymerization, significantly increases the density of imprinted PFAS in the resulting MIP-based sensors. We characterize the total amount and the spatial distribution of the imprinted cavities *via* cyclic voltammetry (CV) and X-ray photoelectron spectroscopy (XPS) sputter depth profiling (SDP), respectively. We demonstrate that both properties depend on the nature of the diffusion boundary layer and the identity of the PFAS templating molecules (*i.e.*, perfluorooctane sulfonic acid, PFOS; perfluorohexane sulfonic acid, PFHxS; perfluorobutane sulfonic acid, PFBS). We further show that the cyclic voltammogram during the electrosynthesis can be modeled using finite element analysis to describe the effect of different synthesis scan rates. We anticipate that our results will provide further insights into the development and optimization of PoPD MIP-based sensors for perfluoroalkyl sulfonic acids (PFSA) towards the applications of decentralized sensors.

1. Introduction

Per- and polyfluoroalkyl substances (PFAS) are a diverse class of synthetic chemicals that have widespread uses in consumer, commercial, and industrial products.[1–7] They have also been linked to adverse health effects due to their toxicity, bioaccumulative properties, and environmental persistence.[1,5,8–13] Thus, there is an urgent need to develop decentralized sensors with the capability of large-scale mapping of PFAS to better understand their fate and transport in the environment.[5,6,10] Currently, the United States Environmental Protection Agency (EPA) has approved liquid chromatography with tandem mass spectrometry (LC-MS/MS) as the only analytical technique for quantitative PFAS analysis.[4,9,14–16] While LC-MS/MS provides the gold

standard in terms of selectivity and sensitivity, it is economically prohibitive and requires well-equipped laboratories and trained specialists.[5,7,10,17] The development of reliable, robust, cost-effective, and deployable sensing platforms could significantly advance research, enable rapid detection, and enhance efforts in environmental remediation.[13,18]

Molecularly imprinted polymer (MIP)-based sensors have emerged as a promising alternative for the detection of PFAS.[11,13,19–28] For example, the seminal work of Ugo and coworkers demonstrated an MIP-based sensor with a limit of detection (LOD) of 0.04 nM for perfluorooctane sulfonic acid (PFOS) with minimal interference from other PFAS.[19] Further development by Dick and coworkers led to the detection of hexafluoropropylene oxide dimer acid (HFPO-DA or GenX) with a LOD of 250 fM in surface water.[22] Additionally, Wang and coworkers reported a portable MIP-based sensor for perfluorooctanoic acid (PFOA) with a LOD of 47.4 pM.[28] These successful proof-of-concept sensors have

*Department of Chemical and Environmental Engineering, University of Arizona, 1133 E. James E. Rogers Way, Tucson, Arizona 85721, USA.
E-mail: suchol@arizona.edu*

© 2025 The Author(s). Published by the Royal Society of Chemistry

RSC Appl. Interfaces, 2025, **2**, 1747–1757 | **1747**

demonstrated the potential for rapid and cost-effective detection of several legacy PFAS with appropriate detection limits. However, several performance issues (*e.g.*, sensing reliability, mechanical degradation, and selectivity) must be addressed in order for MIP-based sensors to serve as a viable screening alternative.[13]

The performance of MIP-based sensors depends on several fabrication parameters during the electropolymerization, which controls the resulting physical properties of the polymer film.[29] Recently, our group reported that the fabrication parameters (*i.e.*, potential window, scan rate, molar ratio between the monomer and templating molecules) significantly impact the mechanical and sensing properties of MIP films fabricated from poly(*ortho*-phenylenediamine) (P*o*PD) and templated with PFOS.[13] Notably, we demonstrated that increasing the synthesis scan rate and reducing the ratio between templating molecules and the monomer (PFOS to *ortho*-phenylenediamine, *o*PD) led to improvement in the reproducibility of the sensing signals. This improvement directly correlated with an increase in mechanical robustness and the elastic recovery as measured by atomic force microscopy (AFM)-based nanoindentation. Thus, we further hypothesize that the synthesis scan rate, which controls the size of the diffusion boundary layer,[30,31] dictates the transport of the monomer and the templating molecules during the polymerization, thereby affecting the imprinting efficiency and the spatial distribution of binding sites in the MIP film. We sought to understand this relationship toward creating design principles for MIP-based sensors targeting a variety of PFAS.

In this work, we investigated the influence of the diffusion boundary layer on the molecular imprinting of several perfluoroalkyl sulfonic acids (PFSA) in P*o*PD toward the fabrication of MIP-based sensors. We hypothesized that the thickness of the diffusion boundary layer modulates the relative mass transport between the monomer and templating molecules to the electrode surface, which impacts the distribution and density of the template in the resulting MIP films after polymerization. We first varied the synthesis scan rate to change the diffusion boundary layer thickness during the electrochemical polymerization. We quantified the spatial distribution of PFOS embedded in the MIP films using both electrochemical and spectroscopic measurements. Specifically, we used cyclic voltammetry with a redox mediator to probe the presence of imprinted sites and X-ray photoelectron spectroscopy (XPS) depth profiling to characterize the location of the templating molecules. Additionally, we used finite elemental analysis (FEA) to predict the effects of scan rate during the electrochemical polymerization. Lastly, we evaluated the effects of synthesis scan rate on the imprinting of different PFSA with varying lengths of the fluorinated tail (*i.e.*, perfluorooctane sulfonic acid, PFOS; perfluorohexane sulfonic acid, PFHxS; perfluorobutane sulfonic acid, PFBS).
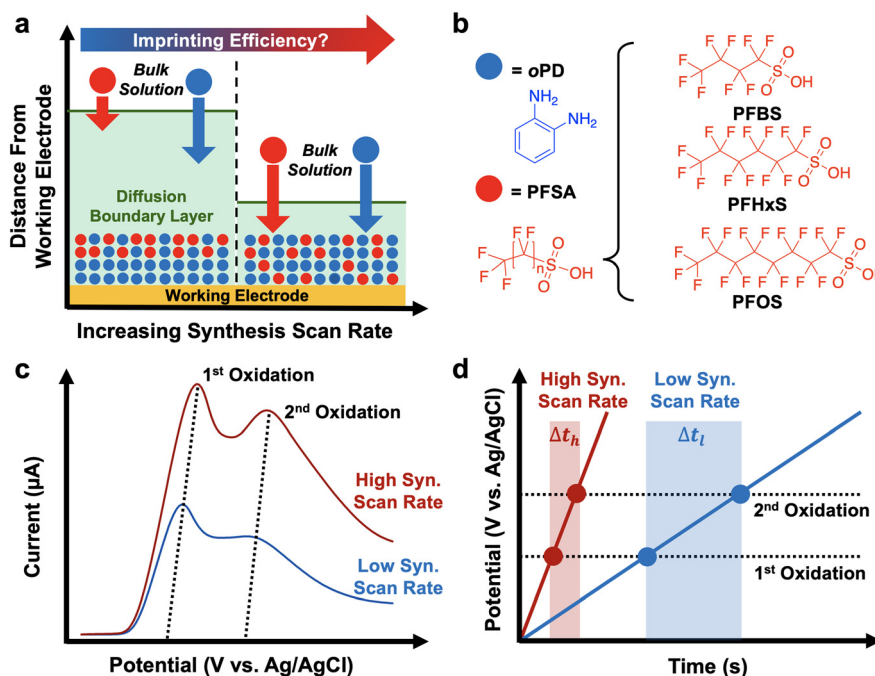

Fig. 1 (a) Schematic of the effects of the diffusion boundary layer on the mass transport of PFSA (red circles) and *o*PD (blue circles) to the electrode during electropolymerization. Higher synthesis scan rate reduces the thickness of the diffusion boundary layer, leading to a higher imprinting efficiency of PFSA. (b) Chemical structures of *o*PD and the three different PFSA used in this study. (c) Representative linear voltammograms (current *vs.* potential) during the electrosynthesis of P*o*PD MIP films at high and low synthesis scan rates. An increase in the total current at high scan rate is attributed to the decrease in diffusion boundary layer thickness and a higher flux of *o*PD toward the electrode. (d) Representation of the electrode potential *vs.* time during an oxidative scan, depicting the time differences between 1st and 2nd oxidations for high and low scan rates.

1748 | *RSC Appl. Interfaces*, 2025, **2**, 1747–1757

© 2025 The Author(s). Published by the Royal Society of Chemistry

2. Experimental design

2.1 Fabrication of molecularly imprinted polymers (MIPs)

We fabricated poly(o-phenylenediamine) (PoPD) MIP films from a solution of o-phenylenediamine (oPD) with PFSA as the templating molecule using methods adapted from previous reports.[13,19,27,32] Briefly, all MIP films were prepared using anodic electrochemical polymerization in acetate buffer containing 10 mM oPD and 0.25 mM PFSA via cyclic voltammetry by scanning 25 cycles in the potential range from 0 to 1.25 V (vs. Ag/AgCl). To test the hypothesis that the thickness of the diffusion boundary layer controls the relative transport rates of the monomer (i.e., oPD) and the templating molecules (i.e., PFSA) to the electrode surface (Fig. 1a and b), we varied the synthesis scan rates (i.e., 50, 100, 150, and 200 mV s^{-1}) to generate different MIP formulations. We focused on tuning the synthesis scan rate because it has been previously shown to control the thickness of the boundary layer,[30,31] the physical properties,[33,34] and the mechanical and sensing properties of MIP-based sensors.[13] Specifically, it influences both the reaction kinetics and mass transport of the electroactive species during the electropolymerization.[29,31] For example, Fig. 1c depicts representative linear voltammograms of two different syntheses of MIP films templated with PFOS at high and low scan rates. With a higher scan rate, the total current increases due to the shrinkage of the diffusion boundary layer, which led to a higher flux of the electroactive oPD toward the electrode.[30,31] Furthermore, we hypothesized that the relative time differences (Δt) between the first and second oxidations of oPD significantly influence the properties of the resulting MIPs.[31,34,35] As shown in Fig. 1d, a higher scan rate would reduce Δt. Thus, we sought to understand the underlying relationship between the synthesis scan rates and the resulting properties of MIP films (e.g., imprinting efficiency). Full details of the synthesis of MIP films are provided in SI, section S1.5. As controls, we also fabricated non-imprinted polymer films (NIPs) using the same parameters without the presence of PFSA.

2.2 Choice of templating molecules

We selected three different PFSA with varying length of the fluorinated tails to evaluate the effects of molecular size on the imprinting efficiency into MIP films. Thus, we chose PFBS (4-carbon tail), PFHxS (6-carbon tail), and PFOS (8-carbon tail) as the templating molecules. We hypothesized that the longer fluorinated tails would increase the hydrophobic interactions with the aromatic oPD monomer and lead to higher imprinting efficiency during polymerization. Additionally, PFSA with longer fluorinated tails have been shown to possess higher surfactant effectiveness, which leads to more favorable surface adsorption.[36–38] We also suspected that the varying synthesis scan rates would have a different impact on the mass transport of each PFSA. Ultimately, we sought to develop a design rule for the fabrication of MIP films using different templating molecules with varying molecular sizes, intermolecular interactions, and surfactant behaviors.

2.3 Electrochemical measurements and characterization

To characterize the MIP-based sensors, we recorded cyclic voltammograms in the presence of a reversible redox mediator, ferrocenecarboxylic acid (FcCOOH), using an indirect sensing strategy.[19,22] We used a 0.1 M ammonia buffer (pH = 8.4) containing 0.5 mM FcCOOH ("redox probe solution") to evaluate the presence of template-free cavities within the MIP films. Specifically, the density of these imprinted cavities can be probed by measuring the current response (i.e., flux of the electroactive redox mediator through the imprinted film to the electrode surface). To differentiate the imprinted cavities from non-specific film defects, we used the differences between the currents measured from MIP films and the NIP controls ("binding site currents"). This value would isolate the confounding effects from differences in film defects and permeability across different fabrication parameters. Full details of the electrochemical experimental procedures are provided in SI, section S1.4.

2.4 X-ray photoelectron spectroscopy sputter depth profiling

In addition to the electrochemical measurement of the imprinted cavities, we used X-ray photoelectron spectroscopy (XPS) with sputter depth-profiling (SDP) to elucidate the spatial location of the imprinted sites within the MIP films.[39] Fig. 2 illustrates the XPS SDP technique where a monochromatized Al K-alpha source (Kratos Axis Ultra 165 hybrid photoelectron spectrometer) irradiated the surface of the MIP films, followed by surface etching using an argon sputtering source for a pre-determined period of time (a pass energy of 1.0 keV and a target current of 10 mA). We sought to minimize the pass energy and target current for each etch to prevent altering the chemical structures of the MIP films (SI, section S9). This process was repeated until the entire MIP film has been fully etched to the gold electrode surface. While conventional XPS surveys provide the elemental analysis of the surface layer, XPS SDP produces atomic concentrations as a function of the film depth. We used the F 1s signature (688 eV) to quantify the presence of the templating molecules and the N 1s signal (400 eV) to represent the PoPD MIP films. We then converted the measured atomic concentration after each etching step to the atomic profile vs. film height, using the measured initial film thickness (KLA-Tencore P15 Profilometer) and the calculated average etch rate for each sample as adapted from previous reports.[39,40]

2.5 COMSOL simulation of MIP electropolymerization

We used COMSOL finite element analysis (FEA) as a comparative simulation tool to evaluate the influence of synthesis scan rate on the mass transport and reaction kinetics during the electropolymerization of MIPs.[31] To

© 2025 The Author(s). Published by the Royal Society of Chemistry
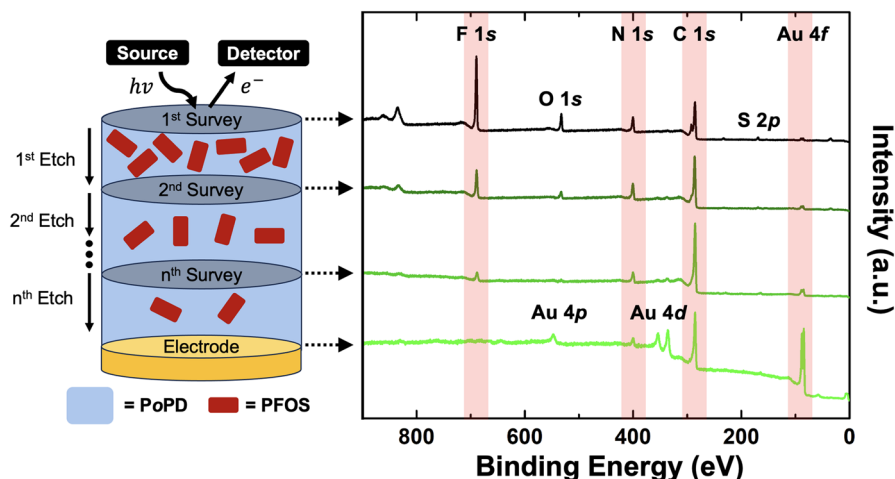
RSC Appl. Interfaces, 2025, 2, 1747–1757 | 1749

Fig. 2 Schematic of the X-ray photoelectron spectroscopy (XPS) sputter depth profiling (SDP) technique of an MIP film imprinted with PFOS. The XPS source irradiates the film to detect the ejected photoelectrons to quantify the elemental composition using the photoelectric effect as shown in the elemental survey trace. After sputter etching of the film, another elemental survey trace is obtained. The cycle of XPS and SDP is repeated until the entire film has been profiled and etched resulting in Au peaks from the surface of the working electrode.

simulate the process, we used the Poisson–Nernst–Planck (PNP) equations to describe both the mass and charge transports in the presence of electric fields and migration. This system of partial nonlinear differential equations is provided in full detail, along with boundary conditions and kinetic models in SI, section S12. To define the stoichiometric relationship during the electropolymerization, we proposed a simplified two-step reaction mechanism adapted from Losito and coworkers comprising (1) the oxidation of oPD and (2) chain propagation with competing oxidative coupling and intramolecular oxidation of the oligomers.[41,42]

3. Results and discussion

3.1 Characterization of MIPs with PFOS as the templating molecules

We began by fabricating four different samples using the same concentrations of the monomers and PFOS at different synthesis scan rates (*i.e.*, 50, 100, 150, and 200 mV s^{-1}). We selected PFOS as the first model study because it has been previously shown to imprint well into PoPD-based MIP films and to produce functional MIP-based sensors.[13,19,27,32] To evaluate the imprinting capacity of each sample electrochemically, we used cyclic voltammetry to measure the changes in the anodic redox peak of a reversible redox mediator (*i.e.*, FcCOOH) as a proxy for the presence of binding sites. Specifically, we collected cyclic voltammograms from (1) the initial bare working electrode (black curves), (2) the MIP films right after synthesis ("pre-template removal", red curves), and (3) the MIP films after the templating molecules were removed *via* solvent extraction ("post-template removal", blue curves) (Fig. 3a). The difference in the measured currents between pre- and post-template removal described

the flux of the redox mediator through the MIP film toward the working electrode. Fig. 3b–e demonstrated the measured cyclic voltammograms from the four MIP films fabricated at different scan rates. We observed that the differences in current monotonically increased with increasing scan rate. Specifically, MIP films fabricated at low scan rate of 50 mV s^{-1} exhibited minimal current differences after post-template removal, unlike the films fabricated at high scan rates (>150 mV s^{-1}). While these results suggested that the amount of PFOS imprinted in MIP films correlated well with the increasing scan rate, the increased current may account for both the formation of selective imprinted cavities and non-specific film defects. That is, structural defects could contribute to the increase in the redox current, potentially leading to an overestimation of the imprinting efficiency. Thus, to deconvolute the contributions from these two effects, we sought to directly measure the presence of PFOS using elemental analysis *via* XPS SDP to map the spatial distribution of the imprinted PFOS in the MIP films. We note here that we observed minor variations in the surface morphology and surface roughness across the MIP films fabricated at different synthesis scan rates. Additional atomic force microscopy (AFM) images and water contact angles are provided in SI, section S15.

To support the results from our electrochemical characterization that suggested a correlation between scan rate and imprinting efficiency of PFOS, we performed an elemental analysis of the MIP films right after synthesis ("pre-template removal"). We used a monochromatized Al K-alpha source for high resolution XPS survey to probe the surface layer with a detection depth of 3 to 5 nm. In order to complete the analysis of the entire MIP films, we performed sequential etching using an argon monatomic ion sputter source, in conjunction with XPS profiling to
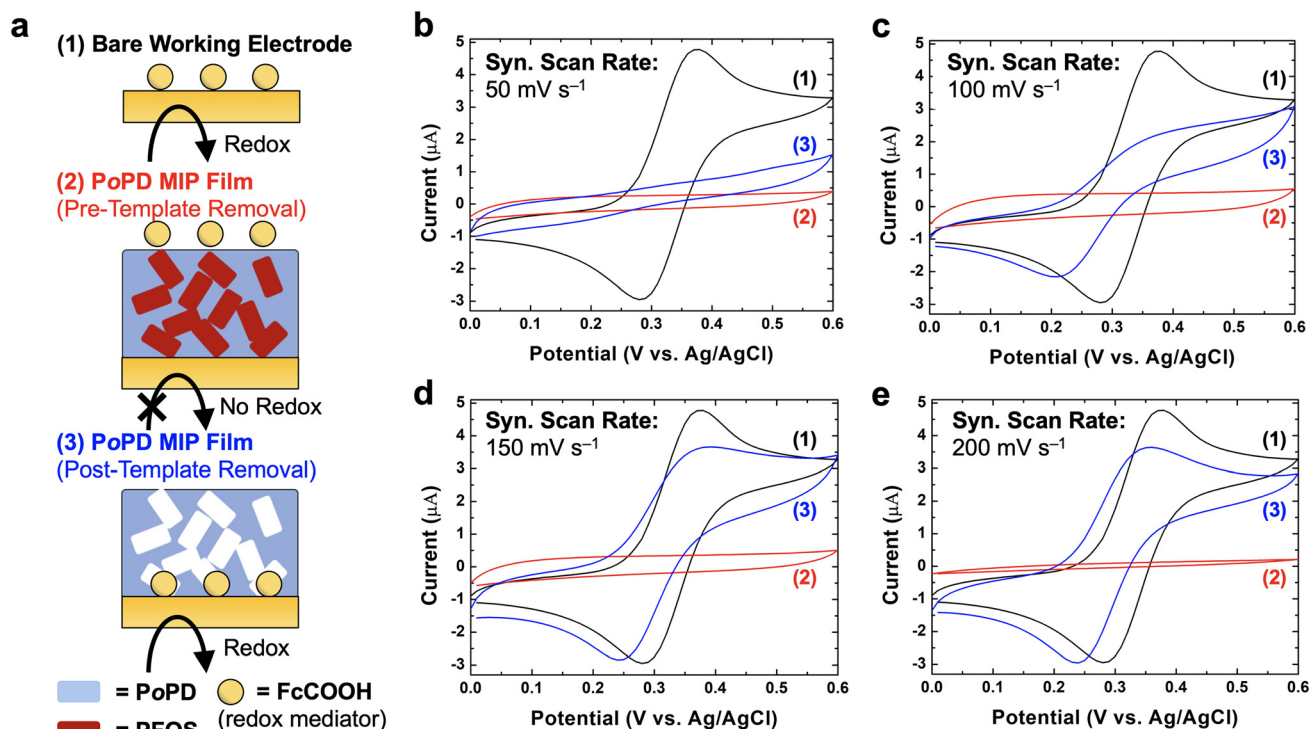
Fig. 3 (a) Schematic of the electrochemical characterization of MIP films imprinted with PFOS, starting with the bare working electrode (black curves), the MIP films right after synthesis ("pre-template removal", red curves), and the MIP films after the templating molecules were removed *via* solvent extraction ("post-template removal", blue curves). (b–e) Representative cyclic voltammograms from MIP films fabricated at the synthesis scan rates ("syn. scan rate") of 50, 100, 150, and 200 mV s^{-1}. All cyclic voltammograms were obtained using a potential window of 0 to 0.6 V *vs.* Ag/AgCl and the measurement scan rate of 50 mV s^{-1}. The representative curves are the averages of five scans. Additional experimental details are provided in SI, section S1.

generate the chemical profiles as a function of the film height. Fig. 4 shows the XPS elemental atomic concentrations of nitrogen (N 1s) and fluorine (F 1s) for the representative samples fabricated using four different synthesis scan rates. We used the N 1s signal to designate the presence of the MIP films and the F 1s for the presence of imprinted PFOS. For all scan rates, we observed that the F 1s photoelectron signature increased with film height. This result implied that the imprinted PFOS was located closer to the top surface of the MIP films and away from the working electrodes. We defined two distinct regions within the MIP films: a PFOS-poor region (F 1s < 1%) and a PFOS-rich region (F 1s > 1%). Interestingly, we observed that the percentage of the PFOS-poor region decreased with increasing scan rate. That is, for the MIP films fabricated at low scan rate (50 mV s^{-1}), the PFOS-poor region extended beyond half of the MIP films. This result provides a stark contrast to MIP films fabricated at high scan rate, where the PFOS-poor regions comprised only a small fraction. We note here that the results in Fig. 4 demonstrated the original film thicknesses, prior to the template removal process *via* solvent extraction with minor variations across the different synthesis scan rates. However, these differences were within the margin of error of the measurement. Similar to previous reports, the film thickness decreased after the template removal process.[13,32]

This reduction is associated with the removal of weakly adhered polymer layers. However, the trend remained consistent when accounting for the final film heights after template removal (SI, section S10). The measurements for the film thicknesses are also provided in SI, section S10.

3.2 Effects of the synthesis scan rate and diffusion boundary layer on imprinting of PFOS into MIPs

Our objective was to evaluate the influence of synthesis scan rate on the imprinting efficiency of PFSA into MIP films. We hypothesized that the diffusion boundary layer controls the relative transport rates between the templating molecules and the *o*PD monomers. As shown previously, the thickness of the diffusion boundary layer can be reduced by increasing the scan rate selected during electrosynthesis.[30,31] Thus, we reevaluated our electrochemical and depth-profiling results from the MIP films imprinted with PFOS using different synthesis scan rates along with the non-imprinted (NIP) controls.

Fig. 5a shows the electrochemical characterization of MIP and NIP films using different scan rates. These reported currents are the magnitudes of the oxidative peak of the redox mediator (~0.35 V *vs.* Ag/AgCl). Similar to the last section, these values account for both the presence of the selective imprinted cavities and non-specific film defects.
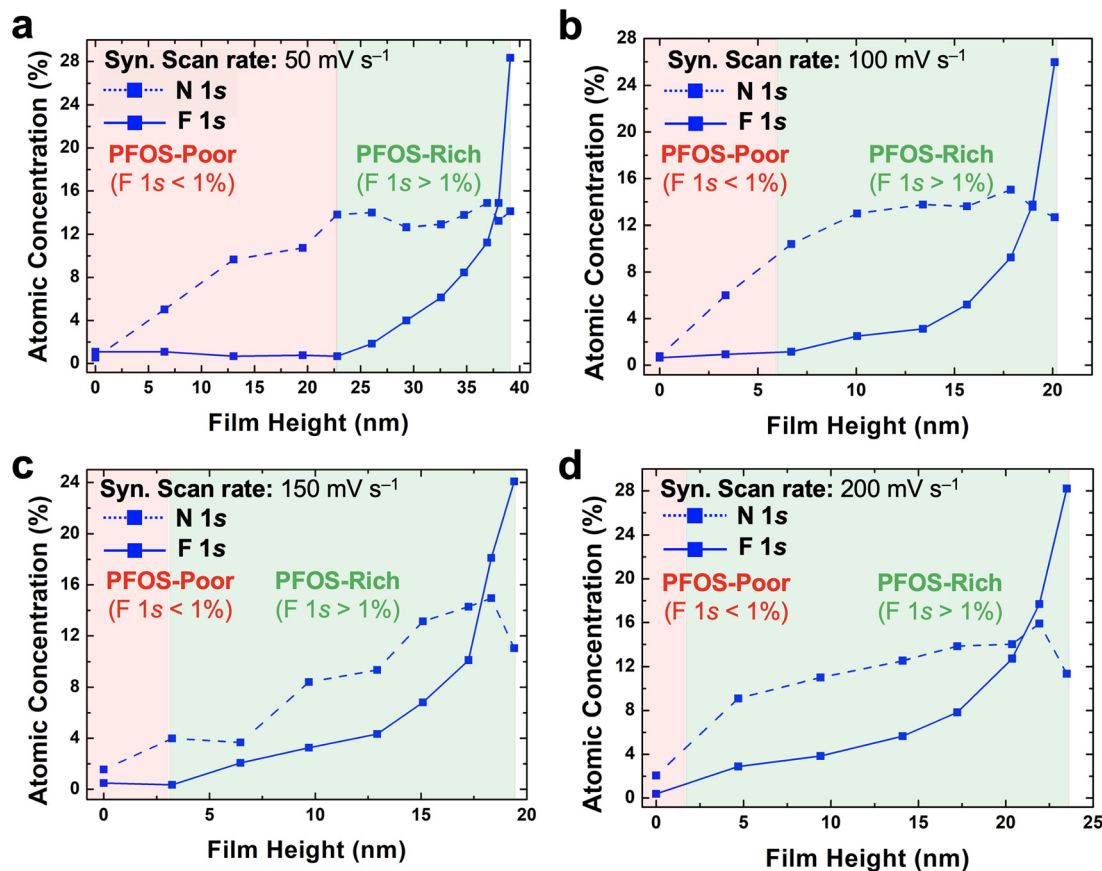
© 2025 The Author(s). Published by the Royal Society of Chemistry

RSC Appl. Interfaces, 2025, **2**, 1747–1757 | **1751**

Fig. 4 Representative elemental analyses using XPS SDP for MIP films imprinted with PFOS using different synthesis scan rates ("syn. scan rate"): (a) 50, (b) 100, (c) 150, and (d) 200 mV s⁻¹. We used the N 1s signal to designate the presence of the MIP films and the F 1s signal for the presence of imprinted PFOS. We defined the PFOS-poor region where the F 1s signal was less than 1% of the atomic concentration, and the PFOS-rich region where the F 1s signal was greater than 1%.
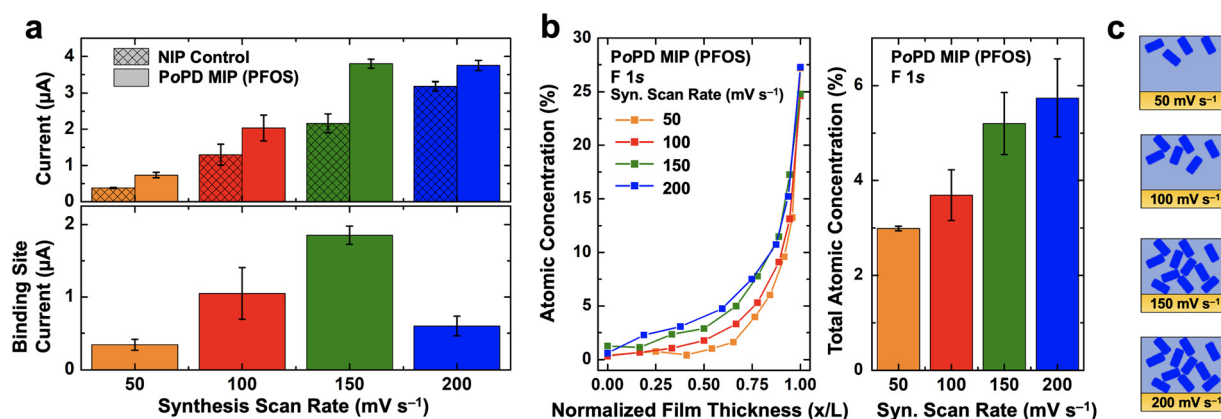

Fig. 5 (a) Electrochemical characterization of MIP films imprinted with PFOS and NIP controls at varying scan rates. The reported current values are the magnitude of the oxidative peak of the redox mediator (FcCOOH, ~0.35 V vs. Ag/AgCl). The binding site current is the difference between the measured currents from MIP films and NIP controls. Values are the averaged values from separate measurements ($N \geq 3$). (b) Normalized XPS depth profiles of the F 1s signal for representative MIP films imprinted with PFOS and the total atomic concentration percentages for the different synthesis scan rates. Values are the averaged values from separate measurements ($N \geq 3$). (c) Schematic representation of the imprinting efficiency of PFOS (dark blue) into PoPD MIP films (light blue).

Thus, we defined a "binding site" current as the difference between the measured currents from MIP and NIP samples to isolate the contribution from non-specific film defects.

First, we observed that the measured currents for both MIP and NIP samples increased with higher synthesis scan rate. That is, there were clear differences between the measured

1752 | *RSC Appl. Interfaces*, 2025, **2**, 1747–1757

© 2025 The Author(s). Published by the Royal Society of Chemistry

currents from films fabricated at 50 and 200 mV s^{-1}. This result suggested that both the imprinting efficiency and film defects increased with increasing scan rate. This trade-off could prove problematic for improving the performance of the resulting sensors, where maximizing binding sites and minimizing film defects are necessary. We attributed these structural defects to the result of reduced time difference between the first and second oxidative events during the electropolymerization of oPD. Second, we observed a local optimal value in the binding site current for MIP films fabricated at 150 mV s^{-1}. These results implied that the imprinting efficiency saturated after a certain synthesis scan rate, while film defects continued to increase. Notably, this also indicated that optimization between maximizing binding sites and minimizing defects is possible by controlling the synthesis scan rate.

We then aggregated the XPS SDP data to demonstrate the effects of the synthesis scan rate (Fig. 5b). We focused on the F 1s signal, which is indicative of the imprinted PFOS, using the normalized film thickness to account for the varying synthesis conditions. As shown by the depth profile and the total atomic concentration, the XPS SDP data generally agreed with the electrochemical characterization. That is, we observed higher PFOS imprinted in MIP films fabricated at higher scan rates. Taken together, both the electrochemical characterization and XPS elemental analysis showed that the choice of synthesis scan rate significantly impacted the formation of the selective binding sites and the spatial distribution of the imprinted PFOS (Fig. 5c). These results also demonstrate an important trade-off between the generation of binding sites and film defects. We previously observed a similar coupled effect when evaluating the mechanical robustness and the sensing performance of MIP-based sensors, where the elastic recovery increased and sensitivity decreased with increasing scan rate.[13] Thus, determining the optimal scan rate that balances the template imprinting efficiency while enhancing desired physical properties is a key design parameter towards advancing MIP-based sensors.

3.3 Modeling the electrosynthesis of MIP films

Next, we sought to develop a predictive model to understand the role of the diffusion boundary layer and synthesis scan rate. The rationales for developing this model were (1) to model the complex process of electrochemical polymerization and (2) to predict and quantify the effects of various physical transport properties (*e.g.*, diffusion coefficients). To this end, we used COMSOL finite element analysis to simulate the experimental cyclic voltammograms during the electrosynthesis of MIP films. Fig. 6a shows the first scan of the experimental voltammograms of the four tested scan rates. The increase in the total current with increasing scan rate was expected due to the decrease in the size of the diffusion boundary layer, promoting the transport of the electrochemically
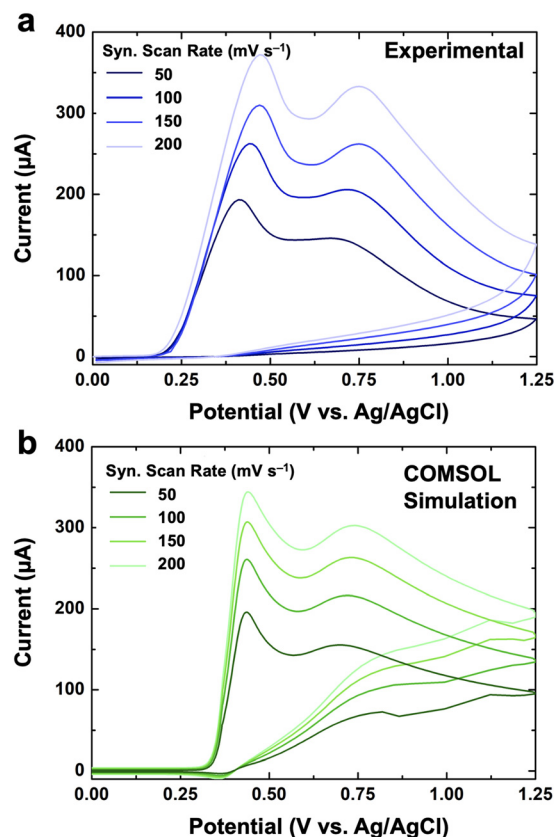

Fig. 6 Cyclic voltammograms (a) from experimental data and (b) from the COMSOL finite element analysis model of the first scan during the electrochemical polymerization of MIP films imprinted with PFOS.

active oPD to the electrode surface. We also observed the two expected oxidation peaks during the polymerization of oPD ($\sim$0.4 V and $\sim$0.75 V *vs.* Ag/AgCl), which were consistent with previous reports.[13,19,26,27] We also observed the reduction of the second oxidative peak ($\sim$0.75 V) with lower scan rates. Interestingly, the magnitude of the second peak ($\sim$0.75 V) has been linked to the interactions between oPD and PFOS (SI, section S11).[13,19,26,27]

Fig. 6b shows the simulated first scan for different scan rates using the Poisson–Nernst–Planck (PNP) equations along with Butler–Volmer kinetics. The simulation produced the expected general trend, showing the increase in current with increasing scan rates. We also observed that it adequately captured the two oxidative peaks during the electropolymerization of PoPD, which corresponded to the initiation step (oxidation of the oPD monomer) and propagation step (oxidation of the oligomeric species).[41,42] Additionally, the simulation captured the passivation of the electrode surface in the cathodic scan due to the growing PoPD film, which was also observed in the experimental data. We note here that we observed several limitations from the simulated waveform. First, the estimated diffusion coefficient of oPD from the simulation (1.25 × 10^{-19} m^2 s^{-1}) indicated poor mobility of the monomers. We attribute this result to the oversimplified Fickian assumptions, which ignore the

© 2025 The Author(s). Published by the Royal Society of Chemistry

RSC Appl. Interfaces, 2025, **2**, 1747–1757 | **1753**

time-dependent diffusion.[43–46] Additionally, the second oxidative peak, corresponding to the propagation of the oligomeric chain, was more influenced by kinetic parameters, particularly the anodic transfer coefficient during propagation (SI, section S13) and the number of electrons during initiation (SI, section S14). These results suggest that the kinetic mechanism for the *o*PD oligomers is missing the necessary complexity to fully describe the MIP polymerization. Despite the kinetic limitations, this simulation provides important insight into the transport and kinetic complexity of the electrosynthesis of the P*o*PD-based MIP, while also highlighting the potential of the PNP comparative model.

3.4 Tuning the molecular imprinting of PFBS and PFHxS

The ultimate goal of this work is to develop a set of design rules to fabricate MIP-based sensors with any choice of templating molecules. To date, only a small subset of PFAS has been successfully implemented into MIP films (*i.e.*, PFOS,[13,19,27] PFOA,[28] and GenX[22]). We hypothesized that PFSA with longer fluorinated tails will result in a higher imprinting efficiency, due to the increased hydrophobic interactions with the *o*PD monomers during the electropolymerization. We also expected that the changes in synthesis scan rate will impact the PFSA disproportionately due to their different interfacial behaviors (*e.g.*, adhesion[47] and adsorption[12,36,37]), which may limit their interactions with the *o*PD monomer.[20,28] Thus, we sought to quantify the imprinting efficiency of PFSA with varying molecular size under different synthesis conditions.

Fig. 7a–c shows characterization of MIP films imprinted with PFBS. The results from both electrochemical and XPS techniques pointed to poor imprinting efficiency of PFBS into P*o*PD. We observed insignificant values of the binding site currents across all tested samples, suggesting that the measured currents were mainly the result of film defects and that the change in the synthesis scan rate had minimal effects on the imprinting process. Moreover, we observed negligible atomic percentage of PFBS *via* the F 1s signal throughout the samples and only minimal values (<2%) at the surfaces of the film. We attributed our results to the poor molecular interactions between PFBS and *o*PD, resulting from the shorter fluorinated tail. Unlike PFBS, PFHxS exhibited a
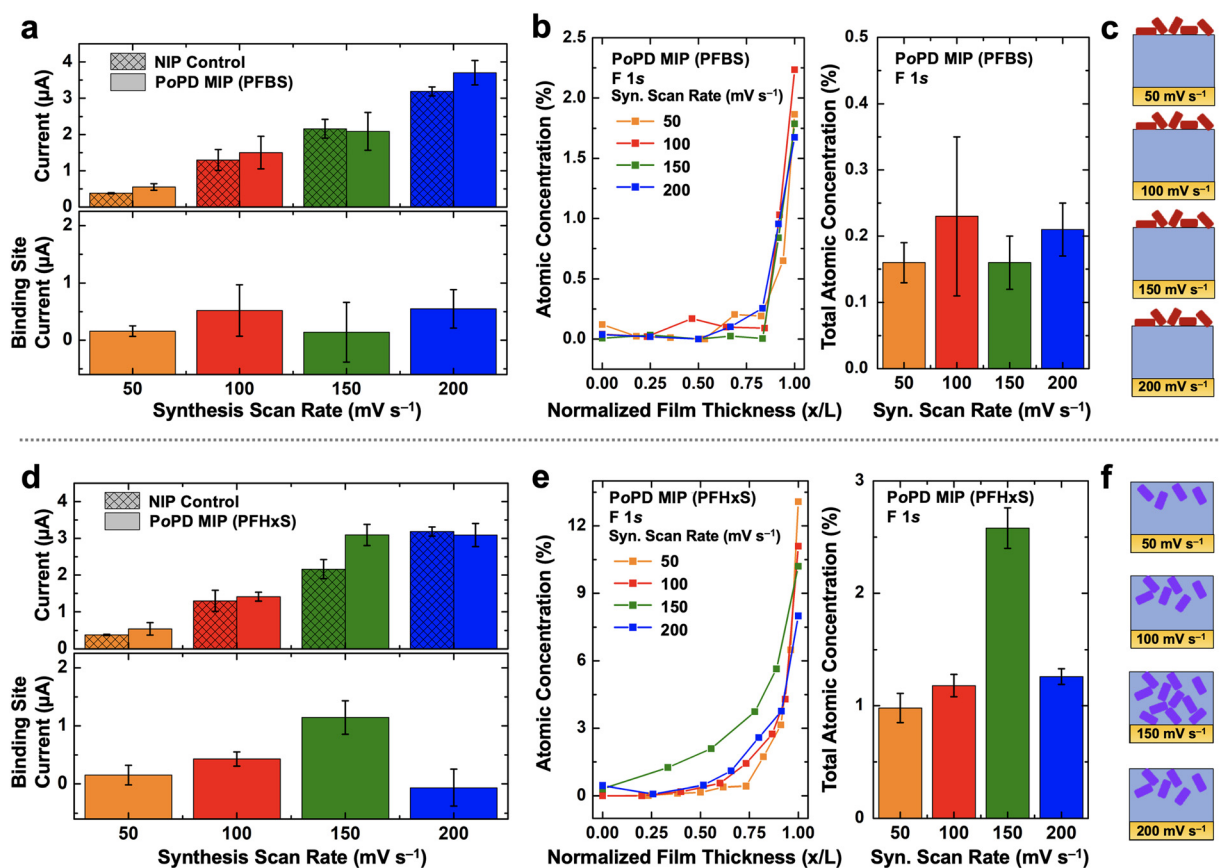

Fig. 7 Electrochemical characterization of MIP films imprinted with (a) PFBS and (d) PFHxS along with the NIP controls at varying scan rates. The reported current values are the magnitude of the oxidative peak of the redox mediator (FcCOOH, ~0.35 V *vs.* Ag/AgCl). The binding site current is the difference between the measured currents from MIP films and NIP controls. Values are the averaged values from separate measurements ($N \geq 3$). Normalized XPS depth profiles of the F 1s signal for representative MIP films imprinted with (b) PFBS and (e) PFHxS with the total atomic concentration percentages for the different synthesis scan rates. Values are the averaged values from separate measurements ($N \geq 3$). Schematic representation of the imprinting efficiency of (c) PFBS (red) and (f) PFHxS (purple) into PoPD MIP films (light blue).
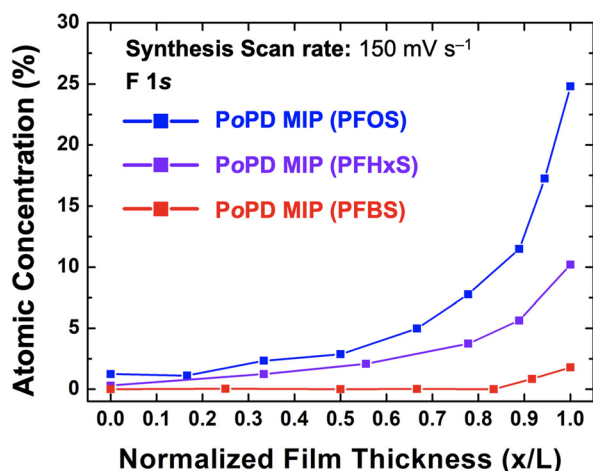
1754 | *RSC Appl. Interfaces*, 2025, **2**, 1747–1757

© 2025 The Author(s). Published by the Royal Society of Chemistry

Fig. 8 Normalized XPS SDP of the F 1s signal for the representative MIP films imprinted with PFOS, PFHxS, and PFBS at the same synthesis scan rate of 150 mV s⁻¹. Values are the averaged values from separate measurements ($N \geq 3$).

clear optimal imprinting efficiency at a moderate synthesis scan rate of 150 mV s⁻¹ (Fig. 7d–f). That is, we observed clear local maxima for both the binding site current and total atomic concentration using the F 1s signal. These results demonstrated that molecular interactions, as well as the synthesis conditions, influenced the imprinting efficiency of MIP films. Additional control experiments and raw XPS data are also provided in SI, section S7–S10. We also note here that an important design consideration is the relative molecular size between the redox mediator and the templating molecules. Specifically, if the redox mediator is significantly larger than the imprinted cavities, steric hindrance may restrict its access and reduce the measured current. Lastly, Fig. 8a demonstrates the comparative atomic concentration profiles of MIP films fabricated with the three tested PFSAs at a constant synthesis scan rate of 150 mV s⁻¹. We observed a clear correlation between templating efficiency and longer fluorinated tail, most likely due to the increase in hydrophobic characteristic (*i.e.*, eight carbon PFOS > six carbon PFHxS > four carbon PFBS).

4. Conclusion

We report the effects of the diffusion boundary layer, as controlled by the synthesis scan rate, on the imprinting of PFSAs into MIP films. We demonstrated that the synthesis scan rate can be used to modulate the imprinting efficiency of PFOS through electrochemical characterization and XPS depth profiling elemental analysis. Using the finite element analysis based on the Poisson–Nernst–Planck equations, we developed a model that agreed well with the experimental data. We also observed clear differences in the imprinting efficiency from PFSA with varying fluorinated tails. Specifically, increasing hydrophobic interactions between the *o*PD monomers and the templating PFSA led to higher imprinting efficiency in MIP films. We note here that the

sensing performance (*e.g.*, selectivity, limit of detection, sensitivity, and stability) of an MIP-based sensor depends on multiple important parameters, in addition to the imprinting efficiency. To provide a fair comparison across the tested samples in this study and to isolate the variable to solely focus on the effects of the synthesis scan rate, we did not perform an optimization to improve the limit of detection. However, we anticipate that our results will provide insights towards the improvement in the development of MIP-based sensors for a variety of PFAS toward the advancement of decentralized environmental monitoring applications.

Data availability

Supplementary information: Experimental details, raw data for electrochemical and XPS characterization, control experiments, measurement of film thickness, surface characterization. See DOI: **https://doi.org/10.1039/D5LF00180C**.

The data supporting this article have been included as part of the SI.

Conflicts of interest

The authors declare no conflict of interest.

Acknowledgements

References

1 S. Garg, P. Kumar, G. W. Greene, V. Mishra, D. Avisar, R. S. Sharma and L. F. Dumée, Nano-Enabled Sensing of per-/Poly-Fluoroalkyl Substances (PFAS) from Aqueous Systems – A Review, *J. Environ. Manage.*, 2022, **308**, 114655, DOI: **10.1016/j.jenvman.2022.114655**.

2 O. June, B. I. Law, P. Acid, P. Sulfonate, U. States, W. Is, H. Advisory, W. Is and N. H. Advisories, *Drinking Water Health Advisories for PFAS Fact Sheet for Communities*, 2022, pp. 2022–2024.

© 2025 The Author(s). Published by the Royal Society of Chemistry

RSC Appl. Interfaces, 2025, **2**, 1747–1757 | **1755**

3   R. C. Buck, J. Franklin, U. Berger, J. M. Conder, I. T. Cousins, P. Voogt, A. A. Jensen, K. Kannan, S. A. Mabury and S. P. J. van Leeuwen, Perfluoroalkyl and Polyfluoroalkyl Substances in the Environment: Terminology, Classification, and Origins, *Integr. Environ. Assess. Manage.*, 2011, **7**(4), 513–541, DOI: **10.1002/ieam.258**.

4   Y. Wang, S. B. Darling and J. Chen, Selectivity of Per- And Polyfluoroalkyl Substance Sensors and Sorbents in Water, *ACS Appl. Mater. Interfaces*, 2021, 60789–60814, DOI: **10.1021/acsami.1c16517**.

5   A. U. Rehman, M. Crimi and S. Andreescu, Current and Emerging Analytical Techniques for the Determination of PFAS in Environmental Samples, *Trends Environ. Anal. Chem.*, 2023, **37**, e00198, DOI: **10.1016/j.teac.2023.e00198**.

6   K. L. Rodriguez, J. H. Hwang, A. R. Esfahani, A. H. M. A. Sadmani and W. H. Lee, Recent Developments of PFAS-Detecting Sensors and Future Direction: A Review, *Micromachines*, 2020, **11**(7), 667, DOI: **10.3390/mi11070667**.

7   United States Environmental Protection Agency, *United States National Primary Drinking Water Regulations*, 2025, **https://epa.gov/dwreginfo/surface-water-treatment-rules**.

8   M. Ateia, A. Alsbaiee, T. Karanfil and W. Dichtel, Efficient PFAS Removal by Amine-Functionalized Sorbents: Critical Review of the Current Literature, *Environ. Sci. Technol. Lett.*, 2019, **6**(12), 688–695, DOI: **10.1021/acs.estlett.9b00659**.

9   Y. Shen, L. Wang, Y. Ding, S. Liu, Y. Li, Z. Zhou and Y. Liang, Trends in the Analysis and Exploration of Per- and Polyfluoroalkyl Substances (PFAS) in Environmental Matrices: A Review, *Crit. Rev. Anal. Chem.*, 2023, **54**(8), 3171, DOI: **10.1080/10408347.2023.2231535**.

10 R. F. Menger, E. Funk, C. S. Henry and T. Borch, Sensors for Detecting Per- and Polyfluoroalkyl Substances (PFAS): A Critical Review of Development Challenges, Current Sensors, and Commercialization Obstacles, *Chem. Eng. J.*, 2021, **417**, 129133, DOI: **10.1016/j.cej.2021.129133**.

11 A. Tasfaout, F. Ibrahim, A. Morrin, H. Brisset, I. Sorrentino, C. Nanteuil, G. Laffite, I. A. Nicholls, F. Regan and C. Branger, Molecularly Imprinted Polymers for Per- and Polyfluoroalkyl Substances Enrichment and Detection, *Talanta*, 2023, 124434, DOI: **10.1016/j.talanta.2023.124434**.

12 V. Trinh, C. S. Malloy, T. J. Durkin, A. Gadh and S. Savagatrup, Detection of PFAS and Fluorinated Surfactants Using Differential Behaviors at Interfaces of Complex Droplets, *ACS Sens.*, 2022, **7**(5), 1514, DOI: **10.1021/acssensors.2c00257**.

13 C. S. Malloy, M. J. Danley, D. A. Bellido-Aguilar, L. Partida, R. Castrejón-Miranda and S. Savagatrup, Effects of Fabrication Parameters on the Mechanical and Sensing Properties of Molecularly Imprinted Polymers (MIPs) for the Detection of Per- and Polyfluoroalkyl Substances (PFAS), *ACS Appl. Polym. Mater.*, 2024, **6**(16), 9914, DOI: **10.1021/acsapm.4c01818**.

14 J. A. Shoemaker and D. R. Tettenhorst, *Epa Document #: Epa/600/R-18/352 Method 537.1 Determination Of Selected Per-And Polyfluorinated Alkyl Substances In Drinking Water By Solid Phase Extraction And Liquid Chromatography/Tandem Mass Spectrometry (Lc/Ms/Ms)*, 2009, vol. 537.

15 J. A. Shoemaker, P. E. Grimmett and B. K. Boutin, *Epa Document #: Epa/600/R-08/092 Method 537. Determination Of Selected Perfluorinated Alkyl Acids In Drinking Water By Solid Phase Extraction And Liquid Chromatography/Tandem Mass Spectrometry (Lc/Ms/Ms) The National Council On Aging*, Senior Environmental Employment Program National Exposure Research Laboratory Office Of Research And Development U. S. Environmental Protection Agency Cincinnati, Ohio 45268, 2009.

16 S. C. Wendelken and U. S. Epa, *Method 533: Determination Of Per-And Polyfluoroalkyl Substances In Drinking Water By Isotope Dilution Anion Exchange Solid Phase Extraction And Liquid Chromatography/Tandem Mass Spectrometry 533-I*, 2018.

17 I. Seguro, P. Rebelo, J. Pacheco, H. Nouws and C. Delerue-Matos, Electrochemical Sensors for Environmental Water Monitoring, in *Biodegradation of Toxic and Hazardous Chemicals*, CRC Press, Boca Raton, 2024, pp. 1–25, DOI: **10.1201/9781003391494-1**.

18 D. Thompson, N. Zolfigol, Z. Xia and Y. Lei, Recent Progress in Per- and Polyfluoroalkyl Substances (PFAS) Sensing: A Critical Mini-Review, *Sens. Actuators Rep.*, 2024, 100189, DOI: **10.1016/j.snr.2024.100189**.

19 N. Karimian, A. M. Stortini, L. M. Moretto, C. Costantino, S. Bogialli and P. Ugo, Electrochemosensor for Trace Analysis of Perfluorooctanesulfonate in Water Based on a Molecularly Imprinted Poly(o-Phenylenediamine) Polymer, *ACS Sens.*, 2018, **3**(7), 1291–1298, DOI: **10.1021/acssensors.8b00154**.

20 R. B. Clark and J. E. Dick, Towards Deployable Electrochemical Sensors for Per- and Polyfluoroalkyl Substances (PFAS), *Chem. Commun.*, 2021, **57**, 8121, DOI: **10.1039/d1cc02641k**.

21 D. Lu, D. Z. Zhu, H. Gan, Z. Yao, J. Luo, S. Yu and P. Kurup, An Ultra-Sensitive Molecularly Imprinted Polymer (MIP) and Gold Nanostars (AuNS) Modified Voltammetric Sensor for Facile Detection of Perfluorooctance Sulfonate (PFOS) in Drinking Water, *Sens. Actuators, B*, 2022, **352**, 131055, DOI: **10.1016/j.snb.2021.131055**.

22 M. W. Glasscott, K. J. Vannoy, R. Kazemi, M. D. Verber and J. E. Dick, μ-MIP: Molecularly Imprinted Polymer-Modified Microelectrodes for the Ultrasensitive Quantification of GenX (HFPO-DA) in River Water, *Environ. Sci. Technol. Lett.*, 2020, **7**(7), 489–495, DOI: **10.1021/acs.estlett.0c00341**.

23 C. Fang, Z. Chen, M. Megharaj and R. Naidu, Potentiometric Detection of AFFFs Based on MIP, *Environ. Technol. Innovation*, 2016, **5**, 52–59, DOI: **10.1016/j.eti.2015.12.003**.

24 L. Zheng, Y. Zheng, Y. Liu, S. Long, L. Du, J. Liang, C. Huang, M. T. Swihart and K. Tan, Core-Shell Quantum Dots Coated with Molecularly Imprinted Polymer for Selective Photoluminescence Sensing of Perfluorooctanoic Acid, *Talanta*, 2019, **194**, 1–6, DOI: **10.1016/j.talanta.2018.09.106**.

25 Z. Jiao, J. Li, L. Mo, J. Liang and H. Fan, A Molecularly Imprinted Chitosan Doped with Carbon Quantum Dots for Fluorometric Determination of Perfluorooctane Sulfonate, *Microchim. Acta*, 2018, **185**(10), 473, DOI: **10.1007/s00604-018-2996-y**.

26 R. B. Clark and J. E. Dick, Electrochemical Sensing of Perfluorooctanesulfonate (PFOS) Using Ambient Oxygen in River Water, *ACS Sens.*, 2020, **5**(11), 3591–3598, DOI: **10.1021/acssensors.0c01894**.

27 R. Kazemi, E. I. Potts and J. E. Dick, Quantifying Interferent Effects on Molecularly Imprinted Polymer Sensors for Per- A Nd Polyfluoroalkyl Substances (PFAS), *Anal. Chem.*, 2020, **92**(15), 10597–10605, DOI: **10.1021/acs.analchem.0c01565**.

28 Y. Wei, H. Liu, S. Wang, K. Yu and L. Wang, A Portable Molecularly Imprinted Polymer-Modified Microchip Sensor for the Rapid Detection of Perfluorooctanoic Acid, *Analyst*, 2023, **148**(16), 3851–3859, DOI: **10.1039/d3an00653k**.

29 J. Heinze, B. A. Frontana-Uribe and S. Ludwigs, Electrochemistry of Conducting Polymers-Persistent Models and New Concepts, *Chem. Rev.*, 2010, **110**(8), 4724–4771, DOI: **10.1021/cr900226k**.

30 N. Elgrishi, K. J. Rountree, B. D. McCarthy, E. S. Rountree, T. T. Eisenhart and J. L. Dempsey, A Practical Beginner's Guide to Cyclic Voltammetry, *J. Chem. Educ.*, 2018, **95**(2), 197–206, DOI: **10.1021/acs.jchemed.7b00361**.

31 A. J. Bard, L. R. Faulkner and H. S. White, *Electrochemical Methods*, Wiley, 3rd edn, 2022.

32 D. A. Bellido-Aguilar, M. Dunmyer, C. S. Malloy, M. J. Danley, V. Karanikola and S. Savagatrup, Effects of Surface Functionalization on the Electrosynthesis of Molecularly Imprinted Polymers (MIPs) and the Detection of per- and Polyfluoroalkyl Substances (PFAS), *RSC Adv.*, 2025, **15**(25), 20341–20349, DOI: **10.1039/D5RA03253A**.

33 A. Yarman and F. W. Scheller, How Reliable Is the Electrochemical Readout of MIP Sensors?, *Sensors*, 2020, **20**(9), 2677, DOI: **10.3390/s20092677**.

34 A. Cot, S. Lakard, J. Dejeu, P. Rougeot, C. Magnenet, B. Lakard and M. Gauthier, Electrosynthesis and Characterization of Polymer Films on Silicon Substrates for Applications in Micromanipulation, *Synth. Met.*, 2012, **162**(24), 2370–2378, DOI: **10.1016/j.synthmet.2012.11.023**.

35 Department of Chemical Engineering and Biotechnology - University of Cambridge, *Linear Sweep and Cyclic Voltammetry: The Principles*, **https://www.ceb.cam.ac.uk/research/groups/rg-eme/Edu/linear-sweep-and-cyclic-voltametry-the-principles**.

36 B. Barua, L. K. Dunham, A. Gadh and S. Savagatrup, Real-Time Detection and Classification of PFAS Using Dynamic Behaviors at Liquid–Liquid Interfaces, *RSC Appl. Interfaces*, 2024, **1**, 1045, DOI: **10.1039/d4lf00128a**.

37 M. Dunmyer, J. Welchert, D. A. Bellido-Aguilar, M. Brusseau, S. Savagatrup and V. Karanikola, Molecular Scale Adsorption Behavior of Per- and Poly-Fluoroalkyl Substances (PFAS) on Model Surfaces, *Chem. Eng. J.*, 2024, **497**, 154286, DOI: **10.1016/j.cej.2024.154286**.

38 L. Zhao, Y. Zhang, S. Fang, L. Zhu and Z. Liu, Comparative Sorption and Desorption Behaviors of PFHxS and PFOS on Sequentially Extracted Humic Substances, *J. Environ. Sci.*, 2014, **26**(12), 2517–2525, DOI: **10.1016/j.jes.2014.04.009**.

39 D. Li, Y. Chen, C. Zhou, C. Shi, Z. Xu, Z. Miao, Z. Xi and J. Han, XPS Depth Profiling of Functional Materials: Applications of Ion Beam Etching Techniques, *Mater. Chem. Front.*, 2023, 715–731, DOI: **10.1039/d3qm01036h**.

40 M. Piskarev, E. Skryleva, A. Gilman, B. Senatulin, A. Zinoviev, D. Syrtsova, V. Teplyakov and A. Kuznetsov, Depth Profile Analysis of the Modified Layer of Poly(Vinyltrimethylsilane) Films Treated by Direct-Current Discharge, *Coatings*, 2021, **11**(11), 1317, DOI: **10.3390/coatings11111317**.

41 I. Losito, E. De Giglio, N. Cioffi and C. Malitesta, Spectroscopic Investigation on Polymer Films Obtained by Oxidation of O-Phenylenediamine on Platinum Electrodes at Different PHs, *J. Mater. Chem.*, 2001, **11**(7), 1812–1817, DOI: **10.1039/b101626l**.

42 I. Losito, F. Palmisano and P. G. Zambonin, O-Phenylenediamine Electropolymerization by Cyclic Voltammetry Combined with Electrospray Ionization-Ion Trap Mass Spectrometry, *Anal. Chem.*, 2003, **75**(19), 4988–4995, DOI: **10.1021/ac0342424**.

43 D. De Kee, Q. Liu and J. Hinestroza, Viscoelastic (Non-Fickian) Diffusion, *Can. J. Chem. Eng.*, 2005, 913–929, DOI: **10.1002/cjce.5450830601**.

44 A. Zhokh and P. Strizhak, Crossover between Fickian and Non-Fickian Diffusion in a System with Hierarchy, *Microporous Mesoporous Mater.*, 2019, **282**, 22–28, DOI: **10.1016/j.micromeso.2019.03.016**.

45 D. A. Edwards, Non-Fickian Diffusion in Thin Polymer Films, *J. Polym. Sci., Part B: Polym. Phys.*, 1996, **34**(5), 981–997, DOI: **10.1002/(SICI)1099-0488(19960415)34:5<981::AID-POLB16>3.0.CO;2-7**.

46 W. Koros and D. Punsalan, Polymer Glasses: Diffusion In, in *Encyclopedia of Materials, Science and Technology*, 2001, pp. 7305–7315, DOI: **10.1016/B0-08-043152-6/01301-2**.

47 J. Welchert, M. Dunmyer, L. Carroll, I. Martinez, T. J. Lane, D. A. Bellido-Aguilar, S. Savagatrup and V. Karanikola, Investigation into the Adhesion Properties of PFAS on Model Surfaces, *RSC Appl. Interfaces*, 2024, **1**, 1265, DOI: **10.1039/d4lf00228h**.

© 2025 The Author(s). Published by the Royal Society of Chemistry

RSC Appl. Interfaces, 2025, **2**, 1747–1757 | 1757